Check for updates

Magnetic properties, magnetocaloric effect, and critical behaviors in $Co_{1−x}Cr_xFe_2O_4$

M. A. Islam [ID] and A. K. M. Akther Hossain [ID] *

This research work focuses on the magnetic properties, nature of the magnetic phase transition, magnetocaloric effect, and critical scaling of magnetization of various $Co_{1−x}Cr_xFe_2O_4$ ($x = 0$, 0.125, 0.25, 0.375, and 0.5). The tunability of the magnetic moment, exchange interactions, magnetocrystalline anisotropy constant, and microwave frequency using Cr^{3+} content has been found. The nature of the magnetic phase transitions for all the Cr^{3+} concentrations exhibits as second order which has been confirmed from the analysis of critical scaling, universal curve scaling, and scaling analysis of the magnetocaloric effect. The critical exponent analysis for all samples was performed from the modified Arrott-, and Kouvel–Fisher-plots. These critical analyses suggest that $x = 0.125$, 0.250, and 0.375 samples show reliable results in the magnetocaloric effect with relative cooling power (RCP) values in the range of $128–145$ J $kg^{−1}$. On the other hand, $x = 0.00$, and 0.500 samples exhibit inconsistent RCP values. The universal curve scaling also confirms the reliability of the magnetocaloric effect of the investigated samples.

1 Introduction

Over the past few decades, research on iron oxide compounds like spinel ferrite, hexaferrite, and garnet has become a topic of discussion among scientists, due to their attractive practical applications in magneto-sensing devices, and biotechnology.[1–7] These key topics attracted scientists because these types of compounds exhibit unique magnetic and magnetocaloric effects (MCE).[1–3,8–10] Among all the ferrites, $CoFe_2O_4$ (COF) has been focused on in recent years by academia, the medical sector, and industry due to its remarkable magnetic and MCE properties.[11–19] The structural, magnetic, and MCE properties of COF can be tuned by doping/substituting divalent or trivalent cations.[11,18–24] The tunability of structural parameters due to Cr^{3+} substitution in stoichiometric and non-stoichiometric COF is reported in our earlier literature.[25] It was observed that there are structural defects due to Cr^{3+} substitution. In recent years, a large number of articles have been found on the study of magnetic field (H) and temperature (T) dependent magnetization (M) of various ferrites.[1,4,26,27] Massoudi *et al.* have observed the non-collinear model on Ni–Zn–Al ferrite by comparing the theoretical and experimental magnetic moment calculated from the cation distribution and M–H hysteresis curve, respectively.[1] The paramagnetic moment followed by the Curie–Weiss law and magnetic phase transition temperature has been studied from the field cooled (FC) and zero fields cooled (ZFC) magnetization.[23,28] Spinel ferrites also attracted scientists across

the world due to their interesting MCE properties.[4,29–32] The MCE is an intrinsic thermodynamic property of magnetic materials that causes a change in the temperature of the substance under the action of a magnetic field.[33] In various literature, the MCE of such materials has been studied from the isothermal M–H over a wide temperature range near the magnetic phase transition.[4,34] The MCE values have been calculated from the change of magnetic entropy from the isothermal M–H curve based on Maxwell's thermodynamic relation.[34,35] The nature of magnetic phase transition has also been reported in various literature extracted from the isothermal M–H curves using the Arrott plot,[36] and the Arrott–Noakes model.[37] Law *et al.* have studied the nature of magnetic phase transition by calculating a critical exponent n from the change of entropy as a function of temperature.[38] Various reports have been conducted on the analysis of critical exponents to confirm the universal class of materials.[32,34] Franco *et al.* have first reported the phenomenological universal scaling curve taking the normalized entropy change as a function of rescaled temperature.[39]

In this research, the effect of Cr^{3+} substitution on magnetic and MCE properties of various $Co_{1−x}Cr_xFe_2O_4$ ($x = 0$, 0.125, 0.25, 0.375, and 0.5) have been studied. A detailed investigation of magnetic properties has been carried out by analyzing the M–H hysteresis and FC-ZFC magnetization behaviors. The MCE properties of Cr^{3+} substituted cobalt ferrite have been investigated by analyzing the M–H isotherms. The nature of magnetic phase transition has also been examined by analyzing the Arrott plot. The nature of the universal class of these materials has been analyzed by calculating the critical exponent followed by

Department of Physics, Bangladesh University of Engineering and Technology, Dhaka-1000, Bangladesh. E-mail: akmhossain@phy.buet.ac.bd

the modified Arrott plot (MAP), the Kouvel–Fisher method, and critical isotherm analysis. Finally, the reliability of the MCE properties and universal class have been studied in detail using as usual methods.

2 Experimental

The nominal chemical compositions $Co_{1-x}Cr_xFe_2O_4$ ($x = 0$, 0.125, 0.25, 0.375, and 0.5) have been synthesized by the standard solid–state reaction technique. The stoichiometric amount of Co_2O_3 (98.0%), Cr_2O_3 (99.9%), and Fe_2O_3 (96.0%) have been mixed in a mortar with a pestle. After completing the mixing process for 2 hours for each composition, the mixtures were crushed using a planetary ball mill (MSK-SFM-1) for 12 h. To complete the solid–state reaction the milled powder has been calcined at 800 °C for 6 h. Then the calcined powder of each composition has been pressed in the form of a pellet using

a uniaxial pressure of 16 000 psi and then sintered at 1200 °C for 6 h. Then a part of sintered pellets was re-crushed into fine powder for performing X-ray diffraction (XRD) to confirm the formation of spinel-type ferrite. The results of phase formation have been reported elsewhere.[25] After confirming the formation of spinel-type ferrites, these compositions are subjected to further investigation of their magnetic properties. The FC and ZFC magnetization were performed for the measurement of the phase transition temperature. The M–H hysteresis loop measurements were performed at room temperature for saturation magnetization and other relevant parameters, The M–H isotherms at a various temperatures above and below the magnetic phase transition for each composition have been conducted by using Quantum Design MPMS3 SQUID magnetometer. Then the MCE properties and critical scaling have been analyzed for each composition using standard method described in Section 3.4.
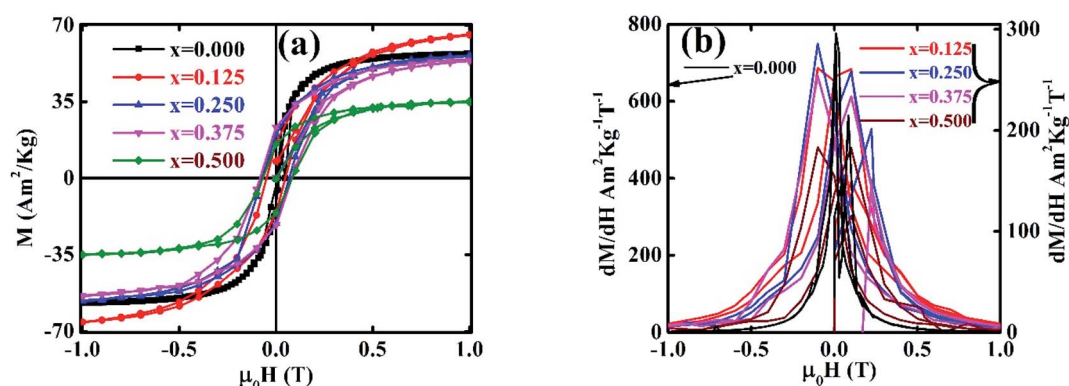

Fig. 1 (a) The room temperature M–H hysteresis loops for various $Co_{1-x}Cr_xFe_2O_4$. (b) The dM/dH versus H plots for various $Co_{1-x}Cr_xFe_2O_4$.

Table 1 Magnetic parameters obtained from M–H hysteresis loops, and M–T curve for various $Co_{1-x}Cr_xFe_2O_4$

Various parameters	x				
	0.000	0.125	0.250	0.375	0.500
θ_{cw} (K)	636	720	710	707	810
C	2.46	1.15	0.89	0.84	0.35
T_C (K)	675	740	735	731	687
T_B (K)	631	685	680	677	671
M_s (A m^2 kg^{-1})	58	70	59	57	37
M_r (A m^2 kg^{-1})	01	19	20	23	15
H_c (T)	0.02	0.05	0.07	0.08	0.07
K (J m^{-3})	1.44	3.6	4.2	4.6	2.2
σ_w (J)	6×10^{-6}	9×10^{-6}	10×10^{-6}	11×10^{-6}	8×10^{-6}
D_m (nm)	78	33	32	31	26
R	0.02	0.268	0.273	0.277	0.306
M_A (μ_B)	5.8	5.7	5.6	5.5	5.4
M_B (μ_B)	10.01	10.07	10.17	10.25	10.34
n_B (μ_B)	2.45	2.94	2.45	2.37	1.51
n_{th} (μ_B)	4.23	4.37	4.56	4.74	4.95
μ_{eff}^{exp} (μ_B)	4.43	3.03	2.66	2.59	1.71
α_{YK} (deg.)	35	31	38	40	48
J (J k^{-1})	1.55×10^{-21}	1.7×10^{-21}	1.69×10^{-21}	1.68×10^{-21}	1.58×10^{-21}
ω_m (GHz)	12.9	15.6	13.0	12.6	8.1

3   Results and discussion

3.1   Structural analysis

The all samples of $Co_{1-x}Cr_xFe_2O_4$ exhibit single-phase cubic spinel structure with a space group of $Fd\bar{3}m$. The details of crystal structure, with cation distribution, have been explored, and results are already published in ref. 25.

3.2   Magnetic properties

The saturation magnetization (M_s), remanent magnetization (M_r), and coercivity (H_c) are the most important parameters for a material to know its magnetic behavior. In general magnetization *vs.* applied magnetic field (M–) hysteresis loop provide

a reliable information about M_s, M_r, and H_c. The M–H hysteresis loops for all samples have been illustrated in Fig. 1(a). From M–H hysteresis loops the values of M_s, M_r, and H_c are extracted and listed in Table 1. From the Table 1, it evident that there is a decreasing trend of M_s with increasing Cr^{3+} content. However, H_c and M_r show the increasing trend up to $x = 0.375$ then it decreases for further increase of x. The decreasing trend of M_s may be due to the abnormal grain growth and pore blockage. The increasing trend of H_c is perhaps due to the decrease in crystallite size (D) as calculated from the XRD data.[25] For $x = 0.500$, the H_c value does not shows the corresponding behavior as crystallite size which may be due to the excess ion as explained in the literature. To know the inter-grain exchange mechanism, the
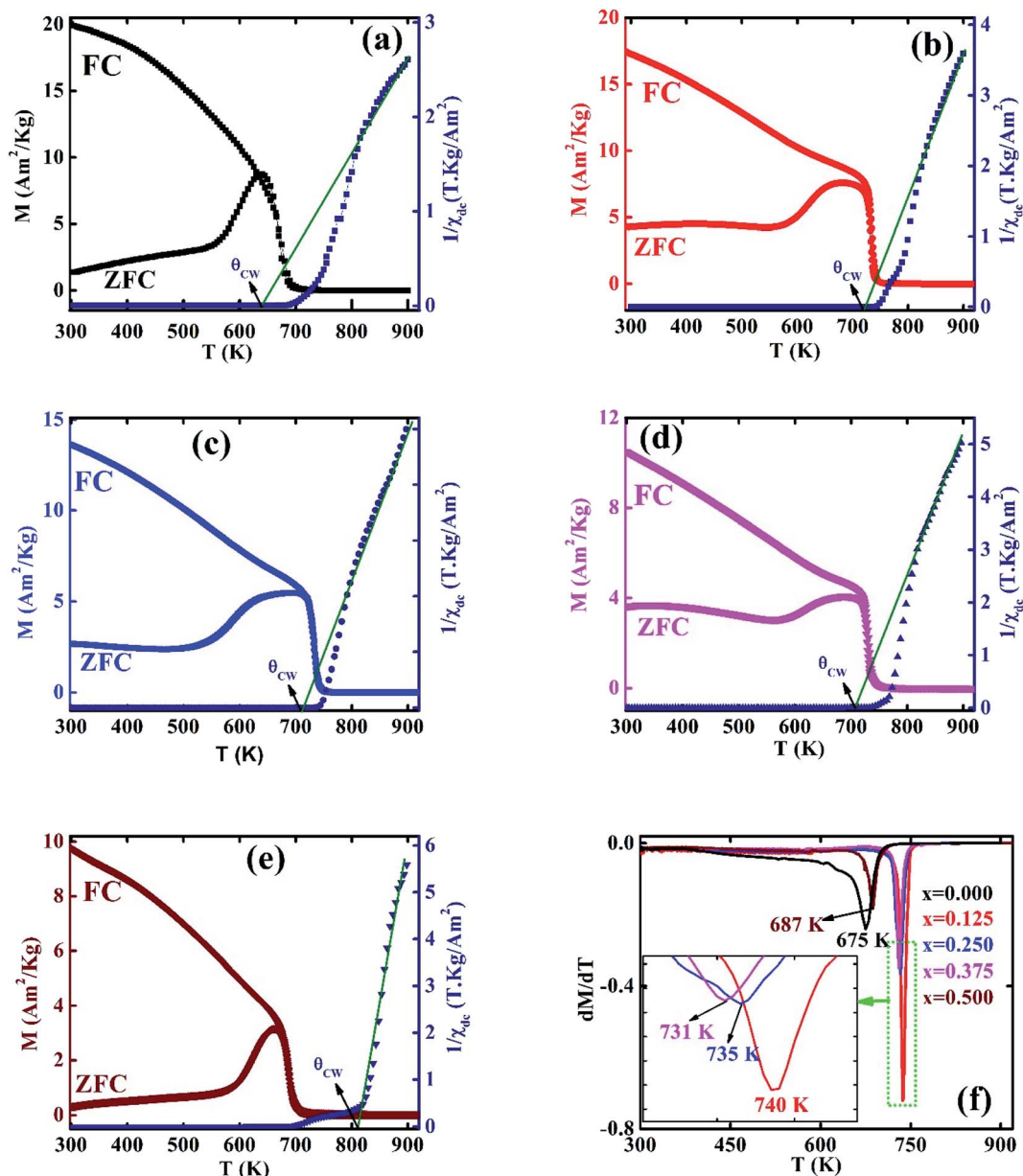

Fig. 2   The temperature dependence of FC and ZFC magnetization (left axis) and the inverse susceptibility (right axis) for various $Co_{1-x}Cr_xFe_2O_4$ (a) $x = 0.0$, (b) $x = 0.125$, (c) 0.25, (d) 0.375, and (e) 0.500. (f) The dM/dT *vs.* T plots for various $Co_{1-x}Cr_xFe_2O_4$.

calculation of remanence ratio R ($= M_r/M_s$) is most important. The calculated R values (Table 1) show less than 0.5 which indicates the existence of magnetic dipole interaction with random orientation.[40] According to Stoner–Wohlfarth theory, the anisotropy constant (K) value is related to the coercivity has been calculated using the following expression:[41]

$$K = \frac{M_s H_c}{0.98} \qquad (1)$$

The calculated K values for all the Cr concentrations are tabulated in Table 1. It is observed from the Table 1 that K values increase with increasing Cr content up to $x = 0.375$, indicating the increase of domain wall energy. Then it shows

the decreasing value which may be due to the excess ions showing negative values of the vacancy parameter as explained in the literature.[25] The domain wall energy (σ_w) can be calculated using the following expression:[42]

$$\sigma_w = \left(\frac{2k_B T_C K}{a}\right)^{\frac{1}{2}} \qquad (2)$$

where k_B is Boltzmann constant, T_C is Curie temperature and a is the lattice constant. The calculated domain wall energy for all samples has been tabulated in Table 1. From Table 1 the values for σ_w are found to be increasing with the increase of Cr content up to $x = 0.375$ then it shows a decreasing trend.
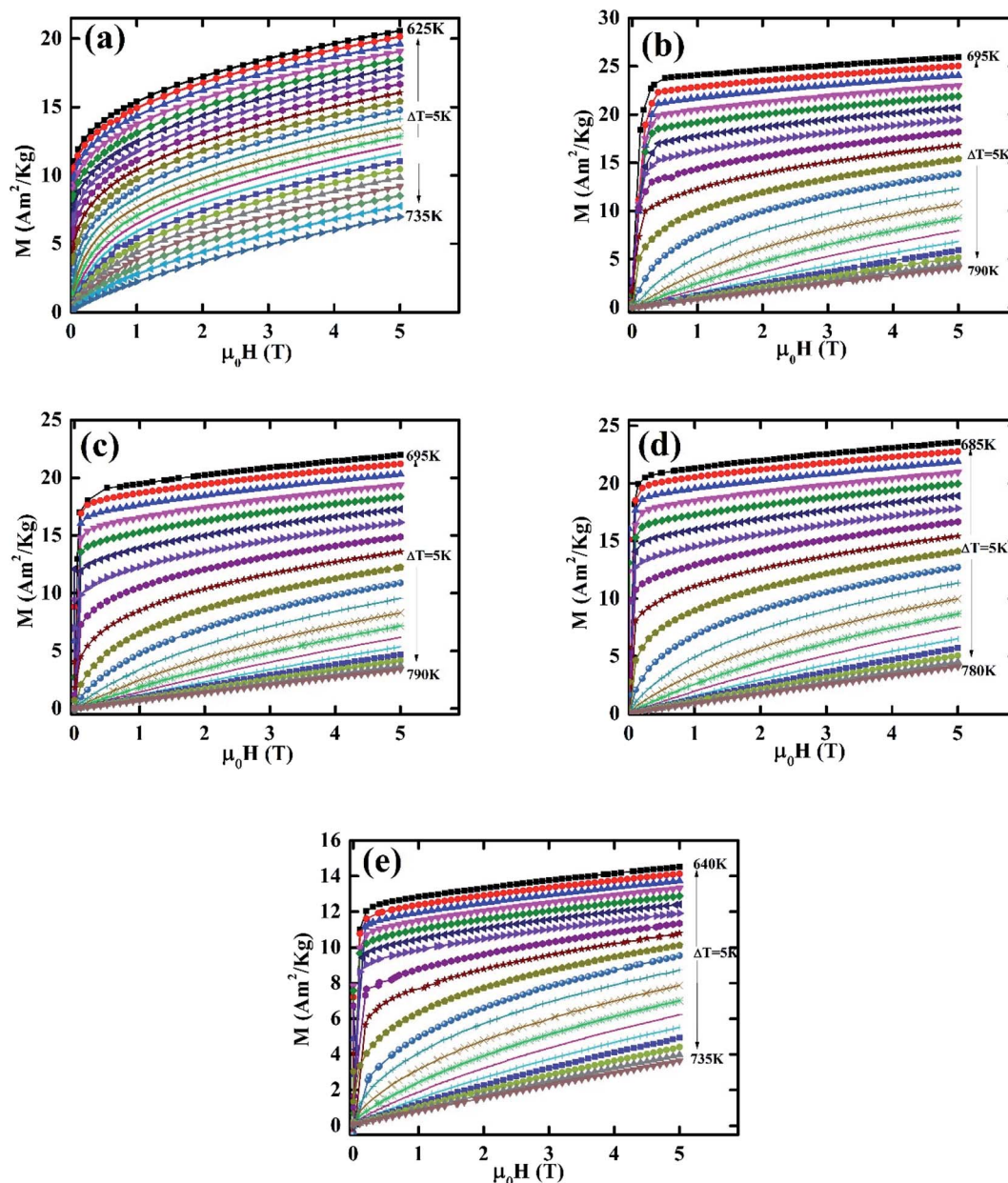

Fig. 3 M–H isotherm for various $Co_{1-x}Cr_xFe_2O_4$. (a) $x = 0.0$, (b) $x = 0.125$, (c) 0.25, (d) 0.375, and (e) $x = 0.500$.
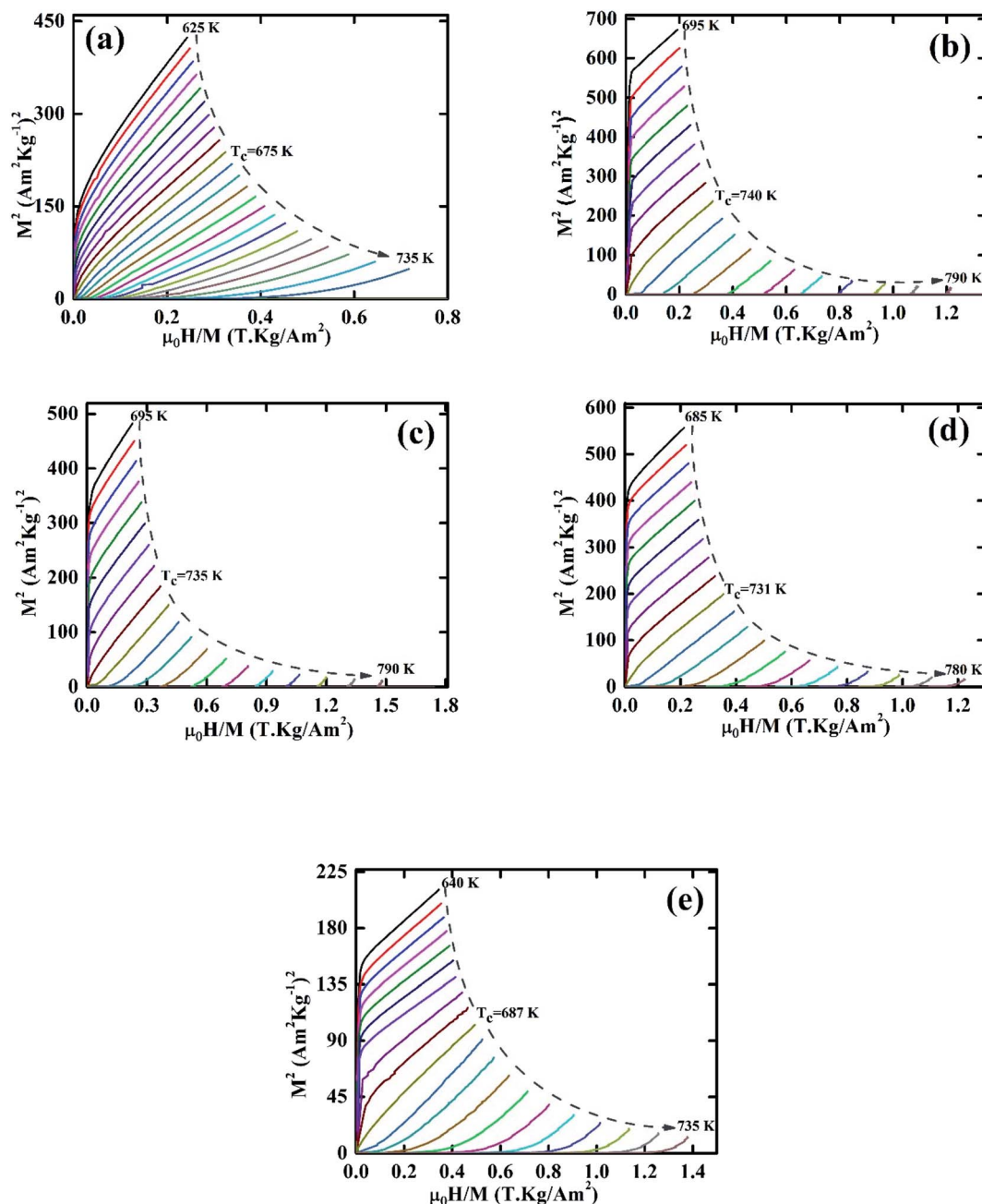
Fig. 4   Arrott plots for various $Co_{1-x}Cr_xFe_2O_4$. (a) $x = 0.0$, (b) $x = 0.125$, (c) 0.25, (d) 0.375, and (e) $x = 0.500$.

To know the domain type of materials, the illustration of the dM/dH versus H plot is most important.[40] The dM/dH versus H for all samples have been depicted in Fig. 1(b). Multiple broad peaks near the zero magnetic field observed for all samples indicate multi magnetic domain. To know the agreeable domain nature, determination of critical size by using the following expression is most important:[43]

$$D_m = \frac{9\sigma_w}{2\pi M_{SP}^2} \qquad (3)$$

where, M_{SP} is spontaneous magnetization. For all samples D_m (Table 1) shows a lower value than the calculated D values from

XRD,[25] which follows the particle spherical model. The $D_m < D$ for all samples reveals that the nanocrystallites have an incipient structure of magnetic domains.[43]

The cation distribution results as presented in our previous article[25] clearly indicate that both Co^{2+} and Co^{3+} occupy the tetrahedral (A) and octahedral (B) sites, respectively whereas Fe^{3+} occupied both the A- and B-sites for $x = 0$. However, for $x = 0.125$ to 0.500, the Cr^{3+} is found in both the A- and B-sites in place of Co^{2+} and Co^{3+}, respectively. The calculated magnetic moment M_A and M_B for A- and B-sites are tabulated in Table 1. From Table 1 the values of M_A are found to be decreasing with an increase of Cr^{3+} which is due to the less magnetic moment of
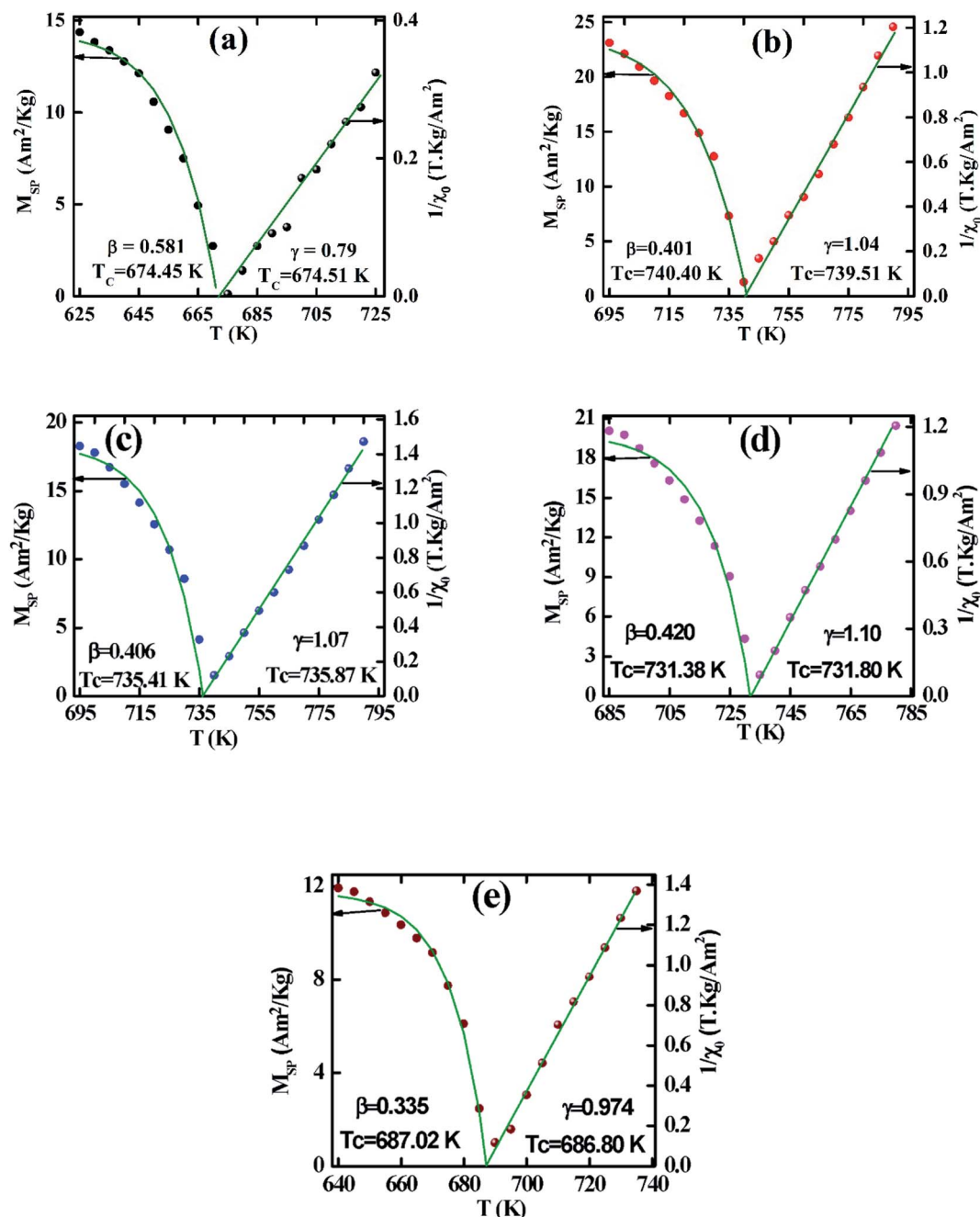
Fig. 5 Spontaneous magnetization M_{SP} and zero field inverse susceptibility χ_0^{-1} as a function of temperature for various $Co_{1-x}Cr_xFe_2O_4$. (a) $x = 0.0$, (b) $x = 0.125$, (c) 0.25, (d) 0.375, and (e) $x = 0.500$.

Cr^{3+} (3.87 μ_B) than Co^{2+} (4.87 μ_B). But the values of M_B are found to be increasing due to an increase of Fe^{3+} with a magnetic moment of 5.92 μ_B. The net theoretical magnetic moment calculated by using $n_{th} = M_B - M_A$ relation accordingly to Néel's co-linear model is tabulated in Table 1. From Table 1, it is observed that the net magnetic moment show an increasing trend which shows inconsistency with the experimental M_s. To know the reason behind the inconsistency the experimental number of Bohr magneton (n_B) is calculated from the value of M_s using the following expression:[1]

$$n_B = \frac{M M_s}{5585} \mu_B \tag{4}$$

where, M is the molecular weight. The calculated values of n_B are also tabulated in Table 1, where lower values of n_B compared to that of n_{th} are evident which suggests that Néel's collinear model is not agreeable for the synthesized samples. For this reason, Yafet–Kittel (YK) non-collinear model is considered to explain the deviation between n_{th} and n_B. According to the YK non-collinear model, the Yafet–Kittel angle (α_{YK}) can be calculated using the following equation:[1]

Table 2 The obtained values of critical exponents (β, γ, and δ) and T_Cs from the modified Arrott plot (MAP), Kouvel–Fisher (KF) plot, critical isotherm, Widom scaling, magnetocaloric effect, and relative cooling power (RCP) analysis across the PM–FM transition region for various $Co_{1-x}Cr_xFe_2O_4$

x	β	γ	δ	n	T_C (K)	Methods
0.000	0.581	0.79	—	—	674.45	MAP
					674.51	
	0.325	1.17	—	0.231	673.37	KF
					673.42	
	—	—	3.23	—	—	Critical isotherm
	—	—	2.34	—	—	MCE/RCP
	—	—	—	0.910	675	$\|\Delta S_m^{max}\|$
	—	—	2.36	—	—	Widom scaling
0.125	0.401	1.04	—	—	740.4	MAP
					739.5	
	0.461	0.998	—	0.676	740.12	KF
					740.09	
	—	—	3.61	—	—	Critical isotherm
	—	—	3.64	—	—	MCE/RCP
	—	—	—	0.677	740	$\|\Delta S_m^{max}\|$
	—	—	3.59	—	—	Widom scaling
0.250	0.406	1.07	—	—	735.41	MAP
					735.87	
	0.464	1.03	—	0.685	734.92	KF
					735.09	
	—	—	3.62	—	—	Critical isotherm
	—	—	3.65	—	—	MCE/RCP
	—	—	—	0.690	735	$\|\Delta S_m^{max}\|$
	—	—	3.63	—	—	Widom scaling
0.375	0.42	1.1	—	—	731.38	MAP
					731.80	
	0.466	1.01	—	0.682	731.32	KF
					730.89	
	—	—	3.60	—	—	Critical isotherm
	—	—	3.61	—	—	MCE/RCP
	—	—	—	0.679	731	$\|\Delta S_m^{max}\|$
	—	—	3.62	—	—	Widom scaling
0.500	0.335	0.974	—	—	687.02	MAP
					686.80	
	0.331	1.08	—	0.422	686.85	KF
					686.89	
	—	—	3.50	—	—	Critical isotherm
	—	—	4.43	—	—	MCE/RCP
	—	—	—	0.501	687	$\|\Delta S_m^{max}\|$
	—	—	3.91	—	—	Widom scaling

$$\cos \alpha_{YK} = \frac{n_B + M_A}{M_B} \quad (5)$$

The α_{YK} values for all the samples are found to be in the range of 30 to 50° (Table 1) which confirms the non-collinear spin structure that indicates triangular spin arrangement in the B-sites. The lower values of Cr^{3+} substitution indicate the decreasing trend of α_{YK} but at higher values of Cr^{3+} enhance the α_{YK}. Although decreasing and increasing trends are evident but they do not show zero α_{YK}. Therefore, the nonzero YK angle suggest that synthesized samples show YK magnetic ordering. The variation of α_{YK} with Cr concentration also support the change in Curie temperature (T_C) as evident from Fig. 2.

The FC and ZFC magnetization plots for all samples were recorded in the presence of 10 mT field in the temperature range of 300–900 K as shown in Fig. 2 (a–e left Y axis). It is evident that the magnetization (M) value in case of ZFC increases up to maximum at a certain temperature for all samples called blocking temperature (T_B) then it shows a decreasing trend with an increase of temperature while the FC magnetization decreases very slowly up to T_C, then a sharp fall is observed for both cases. The values of T_B of all samples are tabulated in Table 1 where maximum T_B value is observed for $x = 0.125$. To know the exact T_C values dM/dT vs. T graphs are illustrated in Fig. 2(f), where a single peak for all samples confirms the single transition at T_C without showing any spin frustration. The T_C values are presented in Table 1. It is observed that T_C show a maximum for $x = 0.125$. With an increase in Cr content, there is a decrease in T_C values. The variation of T_C values and α_{YK} angles of these comositions may be explained by the increasing and decreasing trend of calculated exchange interaction (J) using the following equation:

$$J = \frac{3k_B T_C}{2z \times s(s+1)} \quad (6)$$

where z is the coordination number ($= 12$) and $s = \frac{1}{2}$. The values of J are presented in Table 1.

The inverse magnetic susceptibility (χ^{-1}) as a function of temperature (T) is depicted in Fig. 2 (a–e right Y axis) for all samples. From Fig. 2(a–e) it is found that the χ^{-1} rises sharply when the magnetic state changes from the ferromagnetic to paramagnetic. In the paramagnetic region, susceptibility data follow the Curie–Weiss (CW) expression[34]

$$\chi(T) = \frac{C}{T - \Theta_{CW}} \quad (7)$$

where C is the Curie constant which can be obtained from the slope of the linear fit of χ^{-1} vs. T graph (Fig. 2) and Θ_{CW} is the CW temperature that also can be obtained from Fig. 2. The calculated values of C, and the estimated values of Θ_{CW} from the graphs are listed in Table 1. The estimated values Θ_{CW} are found to be lower than that of T_C for the compositions up to $x = 0.375$ which corresponds to the presence of long-range order. However, for $x = 0.500$ the value of Θ_{CW} is found to be a larger than that of T_C which corresponds to the short-range order which may originate from the excess ion. The experimental effective magnetic moment has been calculated by using C values according to the following expression:[1]

$$\mu_{eff}^{exp} = \sqrt{8C}\mu_B \quad (8)$$

The calculated values of μ_{eff}^{exp} are tabulated in Table 1 where the decreasing trend of μ_{eff}^{exp} with an increase of Cr content has been observed. The decrease in μ_{eff}^{exp} with the increase of Cr^{3+} content may refer to the decrease in ferromagnetic clusters present in the paramagnetic phase.[2]

The microwave frequency (ω_m) is an important parameter for any materials for high-frequency microwave applications. The ω_m can be evaluated by using the following expression:[1,2]
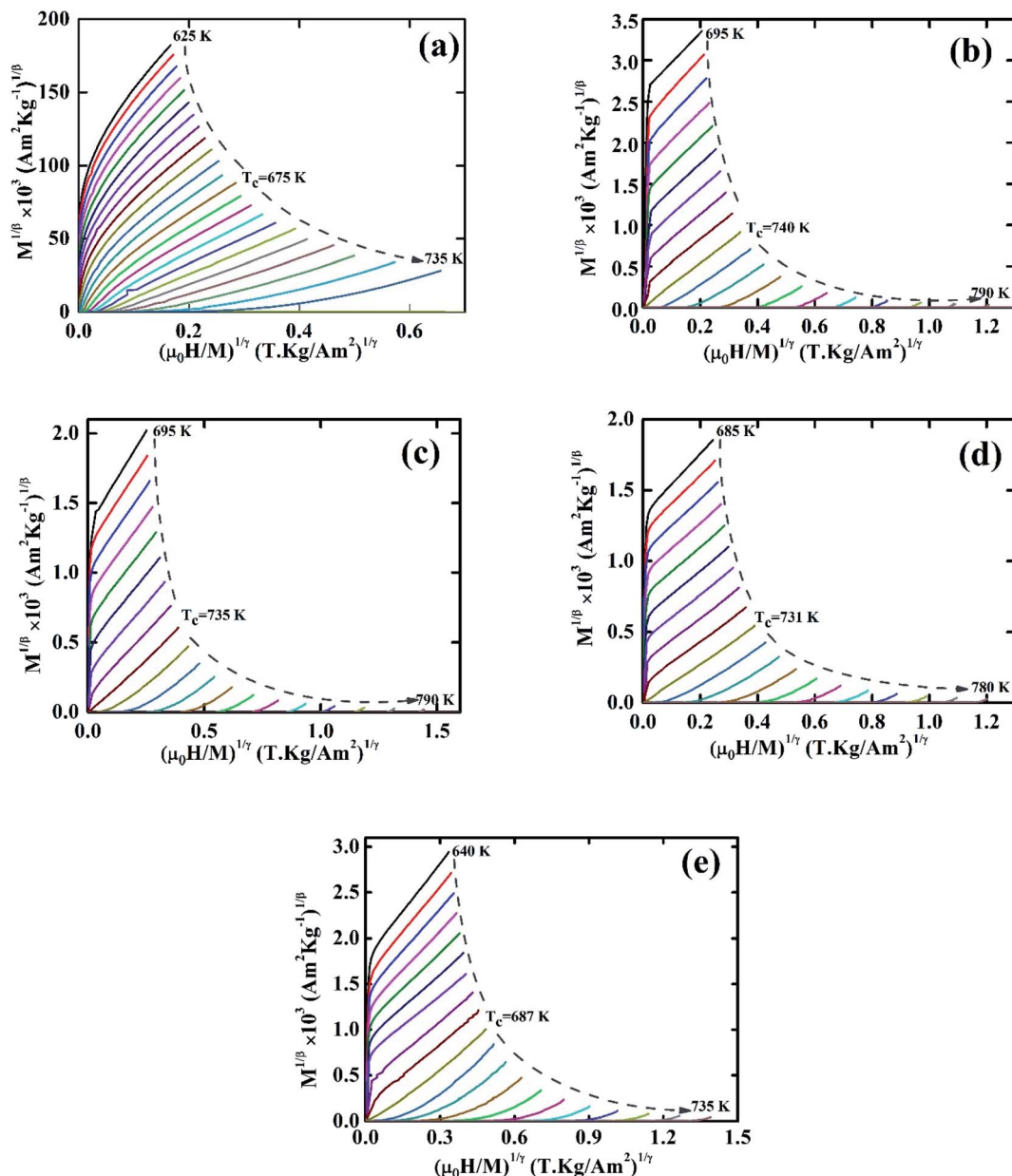
Paper   RSC Advances

Fig. 6   Modified Arrott plot for various $Co_{1-x}Cr_xFe_2O_4$. (a) $x = 0.0$, (b) $x = 0.125$, (c) 0.25, (d) 0.375, and (e) $x = 0.500$.

$$\omega_m = \gamma_1 8\pi^2 M_s \quad (9)$$

where γ_1 is the gyromagnetic ratio ($\gamma_1 = 2.8$ MHz Oe^{-1}). The calculated ω_m values are tabulated in Table 1, where maximum value is observed for $x = 0.125$. The calculated ω_m values are in the range of 8.1–15.6 GHz which is higher than that of previously reported values.[1,2] Thus, it is affirmed that synthesized compositions may be a good candidate for high-frequency microwave applications such as satellite communications and biomedical applications.[44]

3.3   Critical scaling

3.3.1   Modified Arrott plot.
The critical analysis is most important for any inorganic material close to the phase transition. The critical behavior has been conducted by measuring the magnetization isotherms (M–H) close to the respective T_C following the procedure described in ref. 4 and 34. The M–H isotherms for all samples are illustrated in Fig. 3. The non-linear M–H behavior below T_C confirms the compositions are ferromagnetic (FM), and the linear M–H behavior above T_C confirms paramagnetic (PM) nature. Based on the Landau theory, the Gibbs free energy can be written as.[45]

$$G(M, T) = G_o + \frac{1}{2}A_1M^2 + \frac{1}{4}A_2M^4 + \frac{1}{6}A_3M^6 + \dots - \mu_0H \quad (10)$$

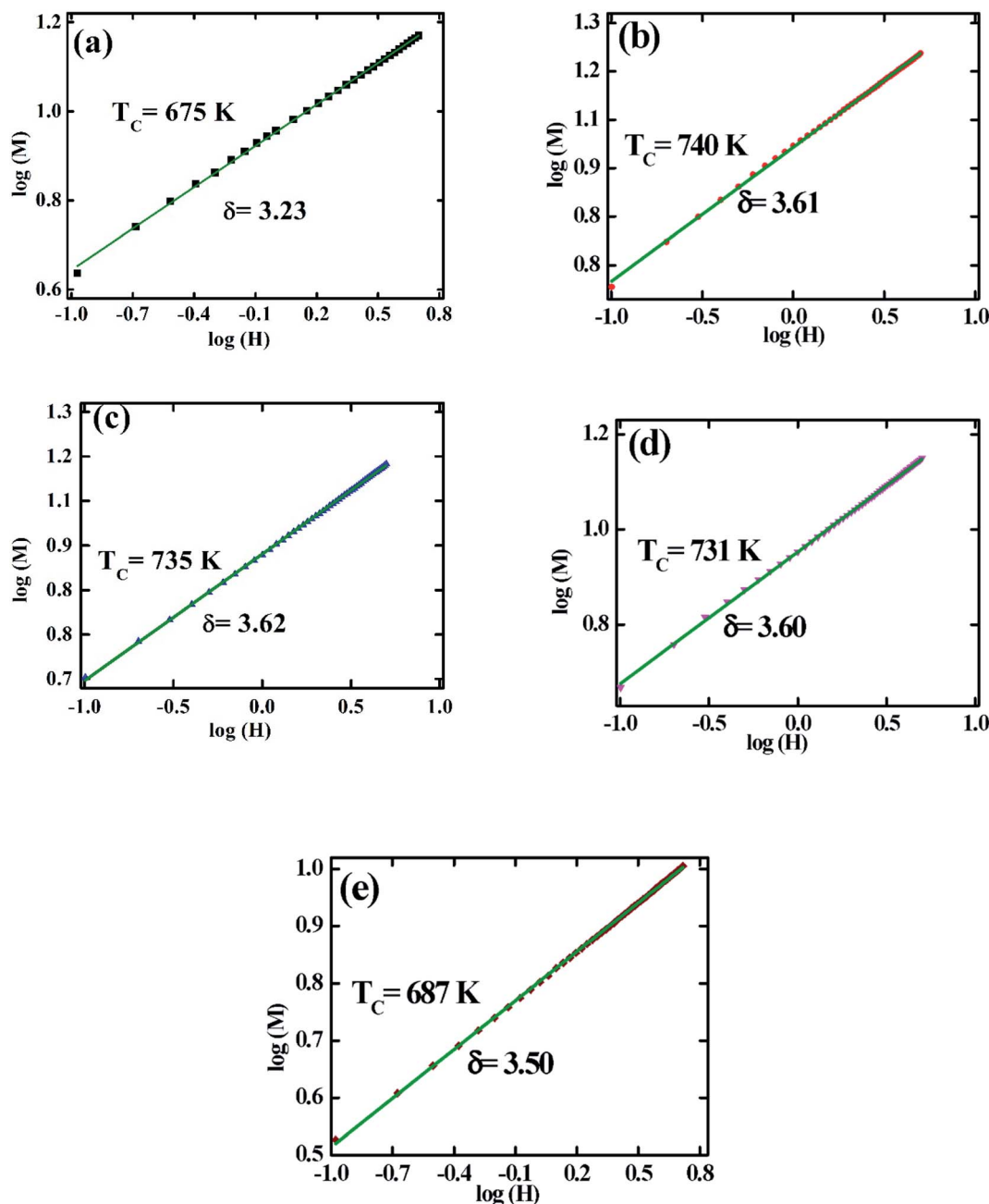where, A_1, A_2, and A_3 are Landau co-efficient. Neglecting the higher-order terms the above equation can be written as

Fig. 7 The log–log plot of isothermal magnetization (M) *vs.* applied field (H) for various $Co_{1-x}Cr_xFe_2O_4$. (a) $x = 0.0$, (b) $x = 0.125$, (c) 0.25, (d) 0.375, and (e) $x = 0.500$.

$$G(M, T) = G_o + \frac{1}{2}A_1 M^2 + \frac{1}{4}A_2 M^4 - \mu_0 H \quad (11)$$

At the equilibrium condition, $\frac{\partial G}{\partial M} = 0$; then the magnetic equation of state can be written as

$$\frac{\mu_0 H}{M} = A_1 + A_2 M^2 \quad (12)$$

The nature of FM–PM phase transition may be determine from the M^2 *vs.* $\mu_0 H/M$, known as Arrott plot.[36] The Arrott plots

for all samples are depicted in Fig. 4. No negative slope has been found in Fig. 4, which confirms the second-order phase transition. It is worth noting that M^2 *versus* $\mu_0 H/M$ plot should follow the equation of straight line passes through the origin. However, the above-mentioned behavior is not observed for all samples. Therefore, further analysis is performed for assumed second-order FM-PM phase transition using modified Arrott plots (MAP) according to Arrott–Noakes[37] as mentioned by the following expression:

$$\left(\frac{\mu_0 H}{M}\right)^{\frac{1}{\gamma}} = A_1 \frac{T - T_C}{T_C} + A_2 M^{\frac{1}{\beta}} \quad (13)$$
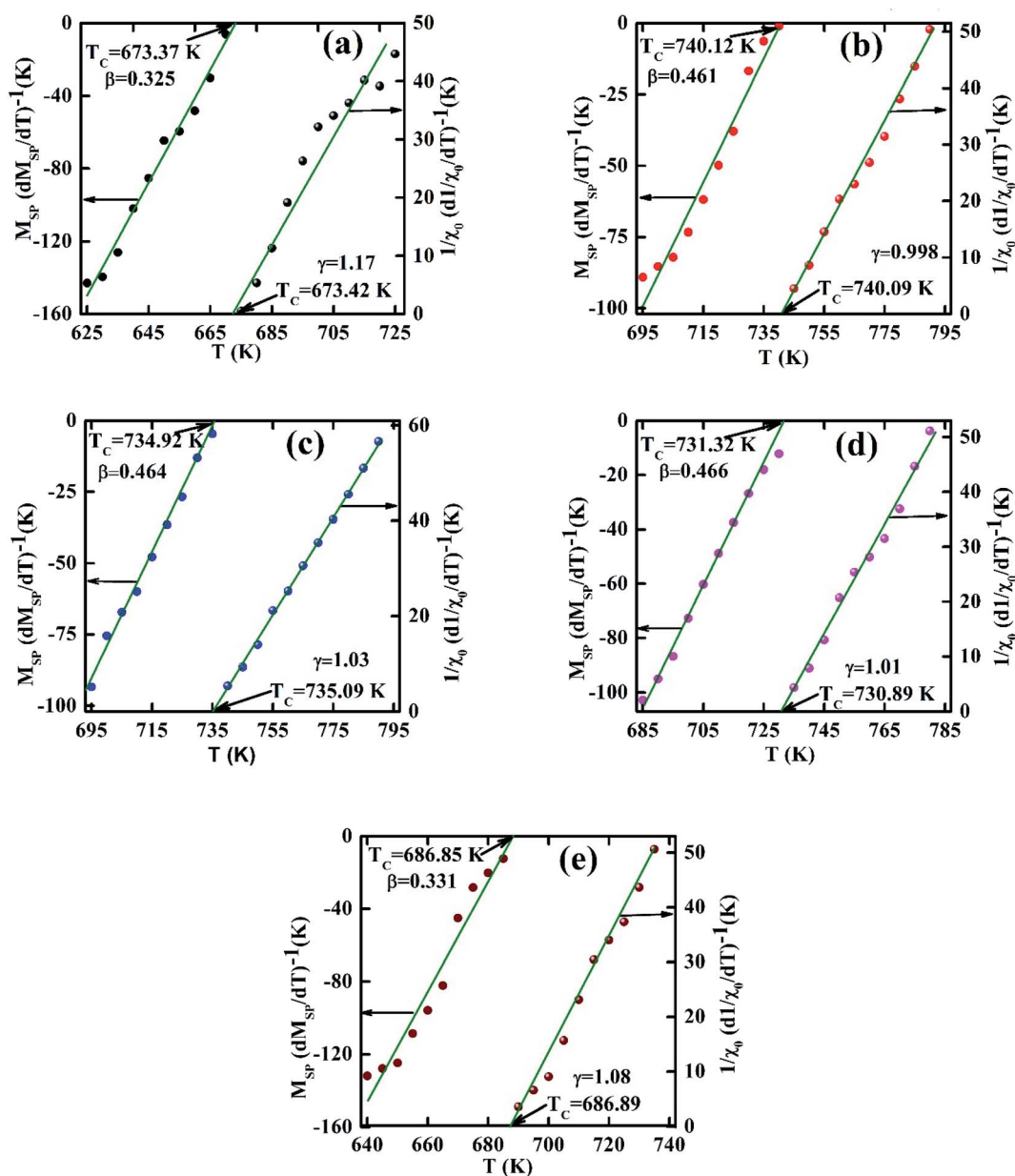
Fig. 8   Kouvel–Fisher plots M_{SP} and χ_0^{-1} as a function of temperature for various $Co_{1-x}Cr_xFe_2O_4$. (a) $x = 0.0$, (b) $x = 0.125$, (c) 0.25, (d) 0.375, and (e) $x = 0.500$.

where β, and γ are the critical exponents.

The set of critical exponents (β, γ, and δ) are calculated by analyzing spontaneous magnetization (M_{SP}), zero-field susceptibility (χ_0), and magnetization isotherm at the T_C using the following power-laws:[4,34]

$$M_{SP}(T) = M_0(-\varepsilon)^{\beta}, \text{ for } \varepsilon < 0, T < T_C, \tag{14}$$

$$\chi_0(T) = \Gamma(\varepsilon)^{\gamma}, \text{ for } \varepsilon > 0, T > T_C \tag{15}$$

$$M = D_1(\mu_0 H)^{1/\delta}, \text{ for } \varepsilon = 0, T = T_C \tag{16}$$

$$M(\mu_0 H, \varepsilon)|\varepsilon|^{-\beta} = f_{\pm}\mu_0 H|\varepsilon|^{-(\beta+\gamma)} \tag{17}$$

where, $\varepsilon = \dfrac{T - T_C}{T_C}$ is the reduced temperature, M_0, Γ, and D_1 are the critical coefficients, and f_+ and f_- are the scaling functions above and below T_C, respectively.

To calculate the values of β and γ (using eqn (14) and (15)) the M_{SP} vs. T, and $1/\chi_0$ vs. T are presented in Fig. 5. From Fig. 5 the β and γ values are estimated from the fitting curve for all the samples that have been tabulated in Table 2. From Table 2 it is found that the values of β and γ are close to the values of the mean-field model for the samples $x = 0.125$, 0.250, 0.375, however, for $x = 0$ and $x = 0.5$, there is a large difference that affects the MCE values as explained in the Section 3.4. The T_C values are also calculated from the fitting curve of Fig. 5 which
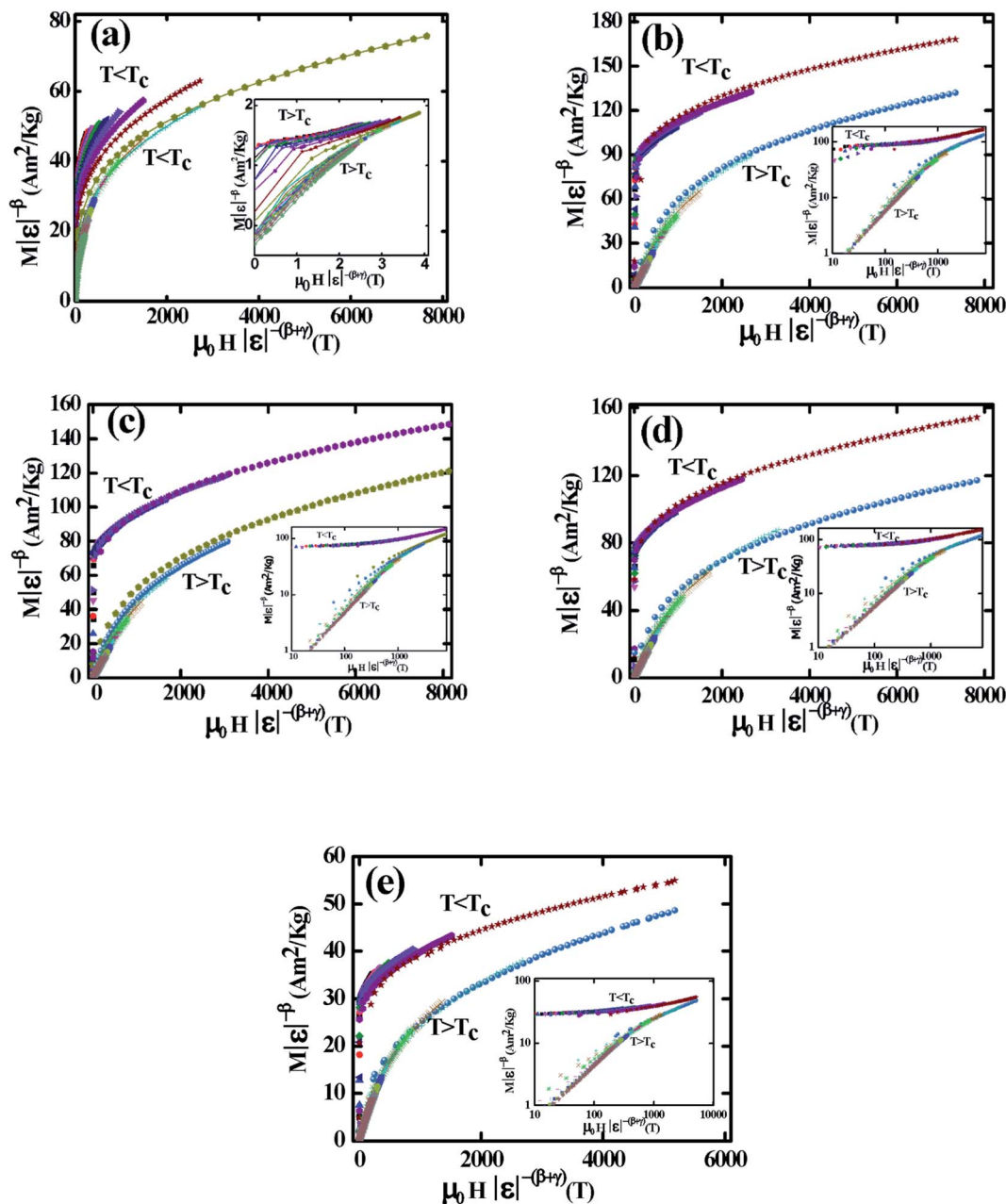
Fig. 9 Scaling plots below and above T_C values using β and γ estimated using the Kouvel–Fisher method. Insets show plots in the log–log scale for various $Co_{1-x}Cr_xFe_2O_4$. (a) $x = 0.0$, (b) $x = 0.125$, (c) 0.25, (d) 0.375, and (e) $x = 0.500$.

also has been tabulated in Table 2 and the values are close to that obtained from M–T measurements described in Section 3.2. The $M^{\frac{1}{\beta}}$ vs. $\left(\frac{\mu_0 H}{M}\right)^{\frac{1}{\gamma}}$ graphs (MAP) for all samples are presented in Fig. 6 using the β, and γ values extracted from Fig. 5. These MAP plots show the straight line that passes through the origin at T_C for $x = 0.125, 0.25, 0.375$, and 0.500 which satisfy the required condition discussed earlier, however, $x = 0$ shows dissimilar behavior.

The variation in the critical isotherm $M(T_C,H)$ can be described by a power-law (eqn (16)) characterized by the critical exponent δ. The critical exponent δ has been obtained from the

inverse of slopes of $M(T_C)$ vs. H curve in the log–log scale as shown in Fig. 7. The δ values are also determined from the previously calculated β, and γ values according to statistical theory using Widom relation:[46]

$$\delta = 1 + \frac{\gamma}{\beta} \qquad (18)$$

The estimated δ values according to the above two cases for all samples are tabulated in Table 2. The δ values for both cases are close to each other for the sample for $x = 0.125, 0.25$, and 0.375 universal class. But for $x = 0.00$, and 0.500 the δ values do not match each other.
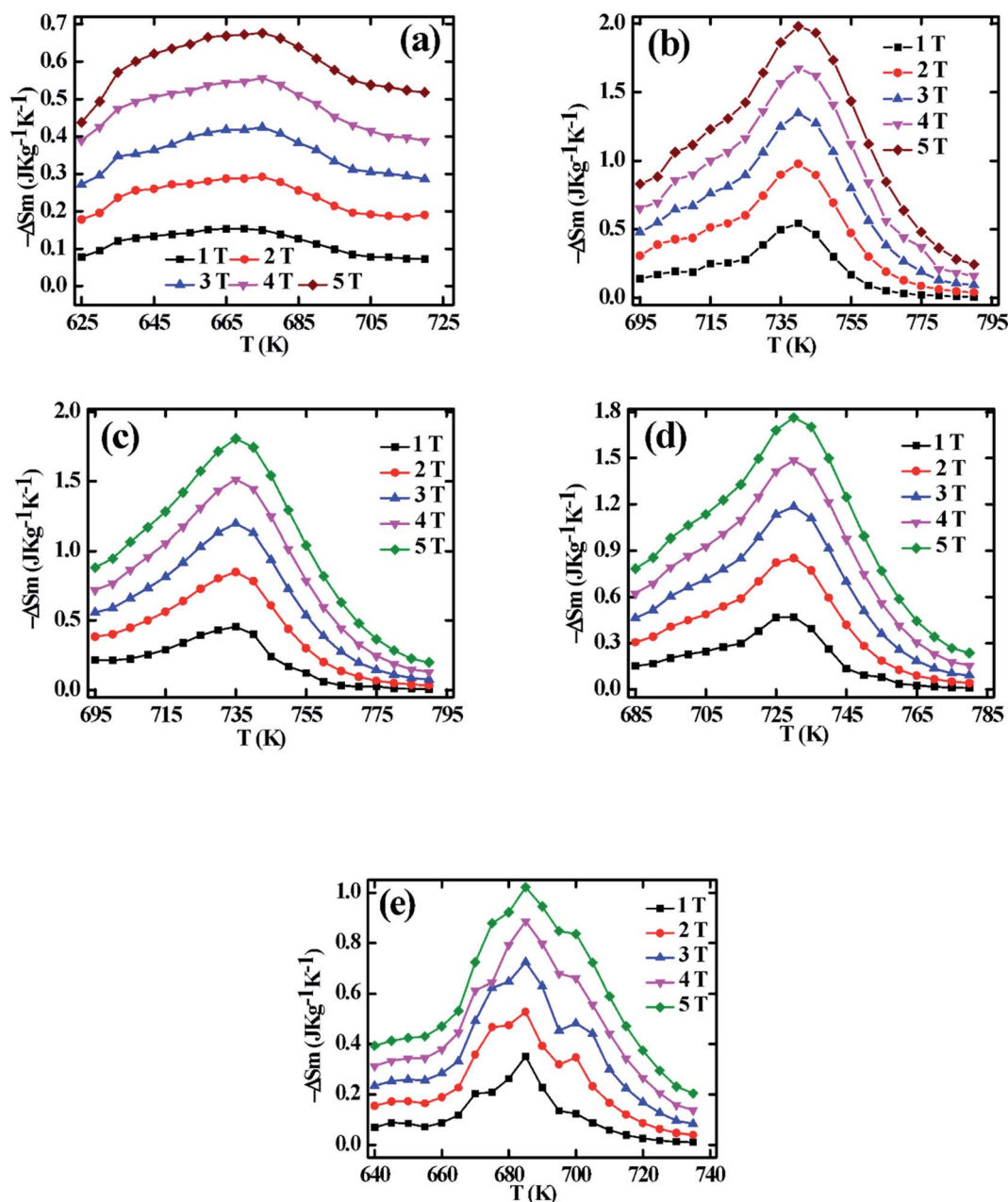
Fig. 10 Magnetic entropy change as a function of temperature for various $Co_{1-x}Cr_xFe_2O_4$. (a) $x = 0.0$, (b) $x = 0.125$, (c) 0.25, (d) 0.375, and (e) $x = 0.500$.

Table 3 Comparison of the Curie temperature, $|\Delta S_m^{max}|$ and RCP for various $Co_{1-x}Cr_xFe_2O_4$ and some other reported samples

| Samples	T_C (K)	μ_0H (T)	$|\Delta S_m^{max}|$ J kg^{-1} K^{-1}	RCP (J kg^{-1})	Reference
$CoFe_2O_4$	675	5	0.66	35.7	This work
$Co_{0.875}Cr_{0.125}Fe_2O_4$	740	5	1.98	128	
$Co_{0.75}Cr_{0.25}Fe_2O_4$	735	5	1.8	137	
$Co_{0.625}Cr_{0.375}Fe_2O_4$	731	5	1.76	145	
$Co_{0.5}Cr_{0.5}Fe_2O_4$	687	5	1.02	52	
$Ni_{0.6}Cd_{0.2}Cu_{0.2}Fe_2O_4$	680	5	2.12	125	Ref. 4
$Zn_{0.4}Ni_{0.2}Cu_{0.4}Fe_2O_4$	565	5	1.41	141	Ref. 29
$Ni_{0.4}Mg_{0.3}Cu_{0.3}Fe_2O_4$	690	5	1.56	136	Ref. 30
$Zn_{0.25}Ni_{0.25}Mg_{0.5}Fe_2O_4$	590	5	1.16	90	Ref. 31
$Mg_{0.6}Cu_{0.2}Ni_{0.2}Fe_2O_4$	670	5	1.38	137	Ref. 32
$Mg_{0.6}Cu_{0.4}Fe_2O_4$	630	5	1.09	136	Ref. 32
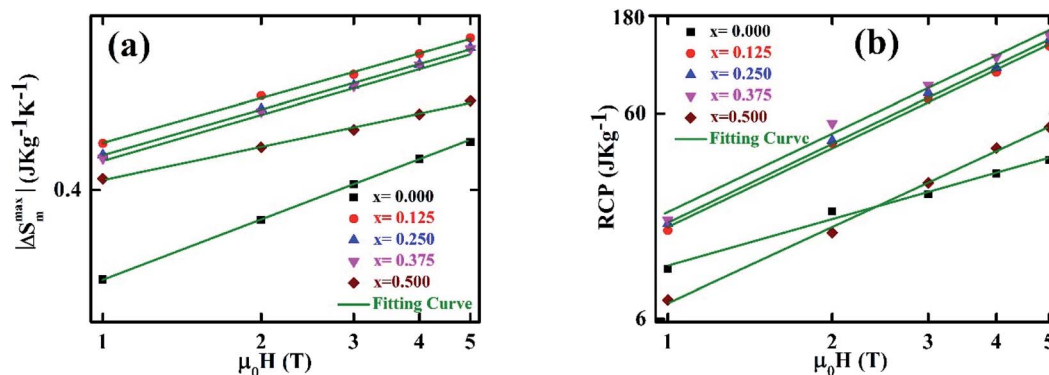
Fig. 11 Magnetic field dependence (a) $|\Delta S_m^{max}|$ at T_C fitted to the power law $|\Delta S_m^{max}| \propto (\mu_0 H)^n$, (b) RCP at T_C fitted to the power law RCP $\propto (\mu_0 H)^{1+1/\delta}$.

3.3.2 Kouvel–Fisher plot. The β, γ, and T_C have been calculated from the Kouvel–Fisher plots (KFPs) that provide more reliable values.[47] In KFPs β, γ, and T_C has been extracted from $M_{SP}\left[\dfrac{dM_{SP}}{dT}\right]^{-1}$ and $\chi_0^{-1}\left[\dfrac{d\chi_0^{-1}(T)}{dT}\right]^{-1}$ *vs. T* graph (Fig. 8) according to the following expressions:[34]

$$M_{SP}\left[\frac{dM_{SP}}{dT}\right]^{-1} = \frac{T - T_C}{\beta} \quad (19)$$

$$\chi_0^{-1}\left[\frac{d\chi_0^{-1}}{dT}\right]^{-1} = \frac{T - T_C}{\gamma} \quad (20)$$

T_C values are extracted from the X-intercepts, and critical β and γ values are obtained from the inverse of slopes of the fitted straight line of Fig. 8. The estimated β, γ, and T_C values for all the samples according to KFPs are tabulated in Table 2, where β, γ, and T_C values are well-matched with the values as the mean-field theory for $x = 0.125$, 0.250, and 0.375. However, for $x = 0.00$, and 0.500 the β, and γ values calculated from KFPs show a remarkable difference compared to that of mean-field theory.

To ensure the reliability of β, γ, and T_C values another robust method have been elucidated by plotting $M|\varepsilon|^{-\beta}$ *vs. $\mu_0 H|\varepsilon|^{-(\beta+\gamma)}$* just above and below T_C according to eqn (17). The $M|\varepsilon|^{-\beta}$ *vs. $\mu_0 H|\varepsilon|^{-(\beta+\gamma)}$* have been plotted for all samples in Fig. 9. The inset in Fig. 9, each case displays the same data plotted on a log–log scale. From Fig. 9, it is evident that two separate groups of isotherms superimpose (one group greater than T_C, and the other group less than T_C) for the samples $x = 0.125$, 0.250, and 0.375. These results suggest the accuracy of β, γ, and T_C values from which it can be decided that these three compositions ($x = 0.125$, 0.250, and 0.375) are a universal class of material. From the inset of Fig. 9, two branches (one below T_C and other above T_C) show the linear behavior in the high field region while in the low field region show some deviation from linearity. These behaviors confirm that the scale theory gives more important data in higher fields. The isotherms for $x = 0.00$, and 0.500 show different behavior that imply the non-universal class of the materials.

3.4 Magnetocaloric effect

The MCE properties is an intrinsic properties of magnetic materials that can be calculated by calculating the magnetic entropy change (ΔS_m) around T_C. The ΔS_m values are calculated from the isothermal M–H data based on Maxwell's thermodynamic relation:[34]

$$\Delta S_m = \int \frac{dM}{dT} dH \quad (21)$$

The calculated ΔS_m for all samples show negative values for all temperature and applied magnetic field. The calculated $-\Delta S_m$ values as a function of temperature are illustrated in Fig. 10 for all samples at different magnetic fields up to 5 T. From Fig. 10, the peak values of $-\Delta S_m$ are defined as maximum entropy change $|\Delta S_m^{max}|$ are evident at T_C or close to T_C. From Fig. 10 it is observed that $|\Delta S_m^{max}|$ increases with an increase of magnetic field are due to the spin ordering for all the samples. The $|\Delta S_m^{max}|$ values are tabulated in Table 3 for 5 T for all samples. Table 3 shows that for $x = 0.125$, maximum entropy change is observed, however, a decreasing trend is found for further increasing of Cr content. The similar behavior is observed for M_s.

Relative Cooling Power (RCP) is another important criterion that helps to characterize the MCE of such magnetic materials. The RCP for all samples has been calculated using the following relation:[4]

$$RCP = |\Delta S_m^{max}| \times \delta T_{FWHM} \quad (22)$$

where δT_{FWHM} is the full width of the $0.5|\Delta S_m^{max}|$. The calculated RCP values are tabulated in Table 3, where very lower values of RCP with lower $|\Delta S_m^{max}|$ for $x = 0.00$ are evident which may be due to the non-universal nature as explained in Section 3.3. For $x = 0.125$, 0.250, and 0.375 it show the comparable values of RCP reported earlier for various ferrite materials.[4,29–32] From Table 3, RCP values are found to increase with the increasing Cr content and found a maximum of 145 J kg^{-1} for $x = 0.375$ which is higher than the previously reported RCP values.[4,29–32] For $x = 0.500$ the RCP values are found to be very low which may be due
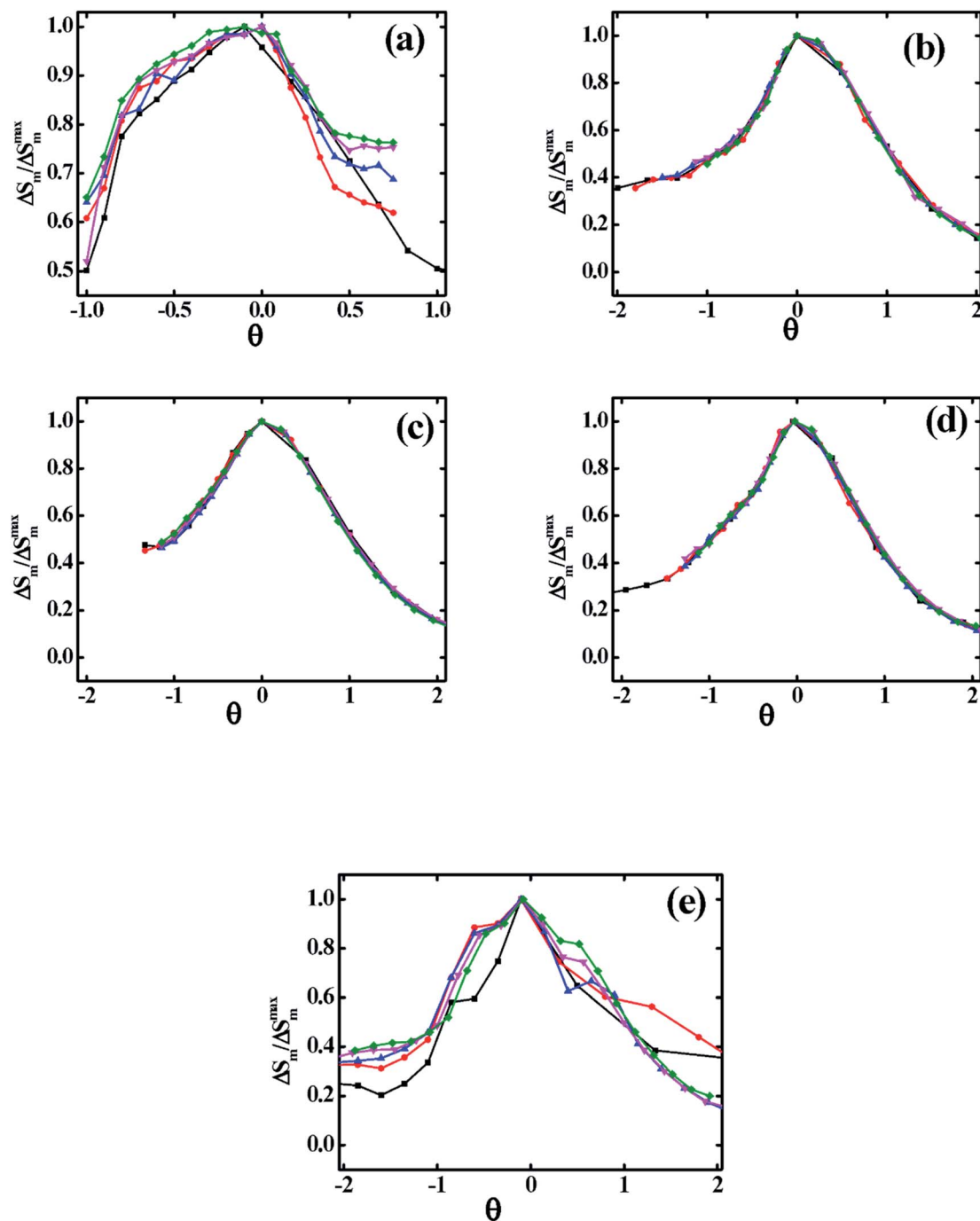
Fig. 12 Normalized magnetic entropy change as function of rescaled temperature for various $Co_{1-x}Cr_xFe_2O_4$. (a) $x = 0.0$, (b) $x = 0.125$, (c) 0.25, (d) 0.375, and (e) $x = 0.500$.

to showing negative values of the vacancy parameter as explained in the previously reported article.[25] Another reason behind showing the lower values of RCP is non-universal behavior for $x = 0.500$.

To analyze the critical exponent, the magnetic field dependent $|\Delta S_m^{max}|$ and RCP are fitted according to the following power law:[38]

$$|\Delta S_m^{max}| \propto (\mu_0 H)^n \qquad (23)$$

$$RCP \propto (\mu_0 H)^{1 + \frac{1}{\delta}} \qquad (24)$$

where, n is the exponent that depends on the magnetic state of the samples. The $|\Delta S_m^{max}|$ vs. $\mu_0 H$ are plotted in the log–log scale and illustrated in Fig. 11(a) for all samples, and the values of n are obtained from the slope of the linear fitting. The obtained n values have been tabulated in Table 2. To explain the reliability of this exponent, calculated the value of n at/near T_C by using the following relation:[34]
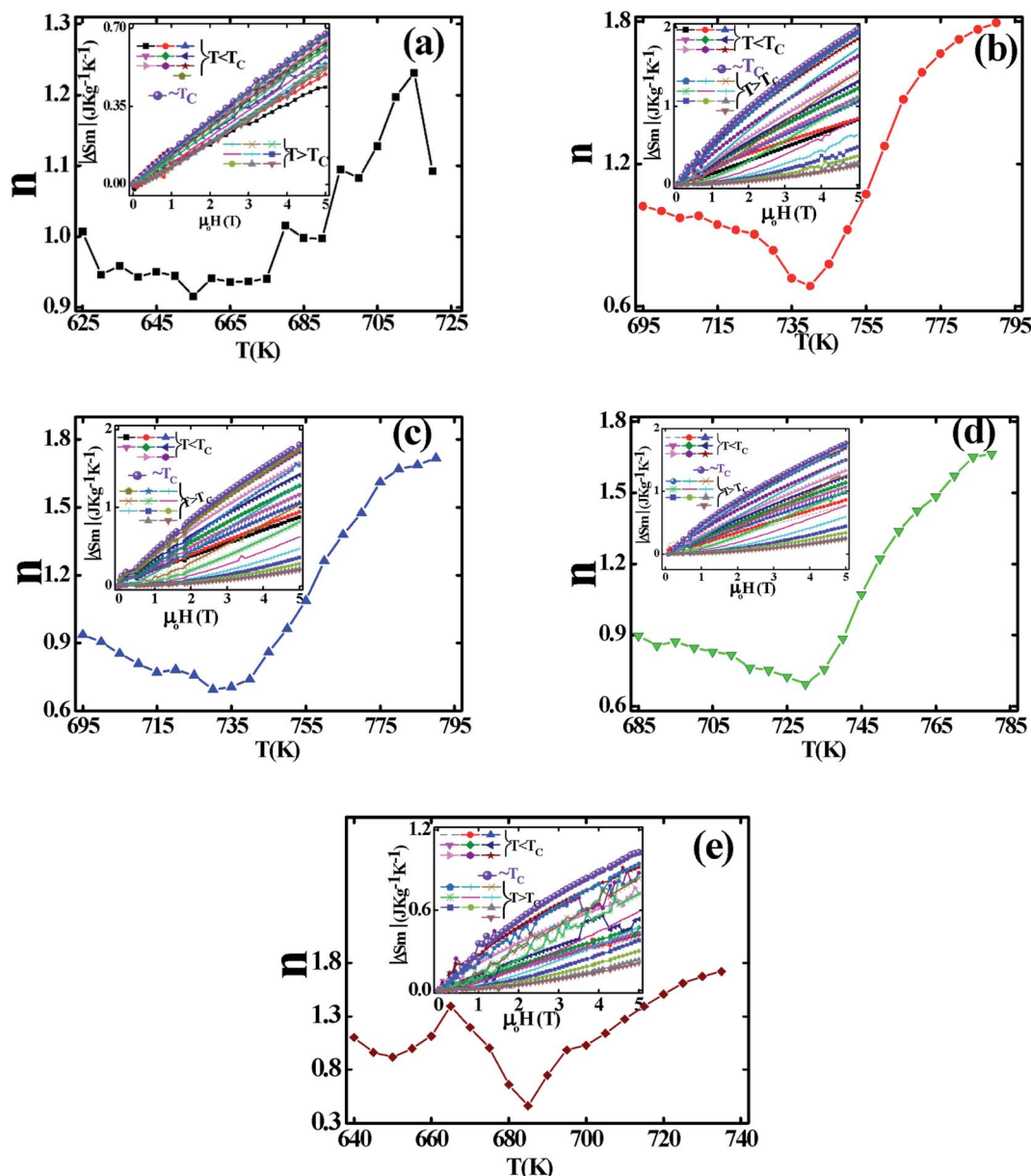
Fig. 13 The exponent n as function of temperature obtained from the fitting of field dependent isothermal magnetic entropy change at various temperature for various $Co_{1-x}Cr_xFe_2O_4$. (a) $x = 0.0$, (b) $x = 0.125$, (c) 0.25, (d) 0.375, and (e) $x = 0.500$.

$$n = 1 + \frac{\beta - 1}{\beta + \gamma} \qquad (25)$$

By applying the Widom relation eqn (18) and (25) can be rewritten as

$$n = 1 + \frac{1}{\delta}\left(1 - \frac{1}{\beta}\right) \qquad (26)$$

The calculated n exponents (using eqn (26)) have been tabulated in Table 2 for all compositions. In this case β and γ values are considered from KFPs, and values of δ are considered from the critical isotherms. The exponent calculated from eqn

(26) are in good agreement with those obtained from the fitted curve of Fig. 11(a) for $x = 0.125$, 0.250, and 0.375. For $x = 0.00$, and 0.500, there is a large difference in the value of n.

The δ values have been obtained from the slope of the linear fit of the RCP vs. $\mu_0 H$ plot in the log–log scale (Fig. 11(b)) according to eqn (24). The obtained δ values by this method are tabulated in Table 2, from where δ values show a good agreement with those of δ values obtained from Widom scaling and critical isotherms for the samples $x = 0.125$, 0.25, and 0.375 (Sec. 3.3). However, for $x = 0.00$, 0.500 a large difference of δ values has been obtained. Comparing the values of n and δ according to Fig. 11, and critical scaling it is decided that the MCE properties of present compositions are reliable.

Verification of critical phenomena and the nature of the magnetic phase transition of these materials are also important. In 2006, Franco et al. have utilized the phenomenological universal scaling curve.[39] According to this method normalized magnetic entropy as a function of re-scaled temperature θ (eqn (27)) has been plotted at several magnetic fields which are depicted in Fig. 12.

$$\theta = \begin{cases} -\dfrac{T - T_C}{T_{r_1} - T_C}, & T \leq T_C \\[2mm] \dfrac{T - T_C}{T_{r_2} - T_C}, & T \geq T_C \end{cases} \quad (27)$$

where, T_{r_1} and T_{r_2} are two-temperatures corresponding to $0.5|\Delta S_m^{max}|$.

In Fig. 12(b–d) it is observed that the results of various magnetic field collapsed into a single master curve, which implies that synthesized samples of $x = 0.125$, 0.250, and 0.375 are in universal class and show exact second-order phase transition.[34] However, from Fig. 12(a and e) it is evident that for $x = 0.00$, and 0.500, samples are non-universal class.

To analyze the accuracy of MCE properties and order of phase transition, the value of n is calculated using the following expression:[38]

$$n(T, \mu_0 H) = \frac{d \ln |\Delta S_m|}{d \ln \mu_0 H} \quad (28)$$

The calculated n values as a function of T are illustrated in Fig. 13 for all samples where the inset depicted the $|\Delta S_m|$ vs. $\mu_0 H$. From the Fig. 13(b–d), it is found that the n values for $x = 0.125$, 0.250, 0.375 are close to 1 below T_C which suggests that the dM/dT term in eqn (21) is weakly field-dependent.[34] With an increase in temperature it is observed the decreasing trend and arrive the minimum n values of 0.684, 0.695, and 0.693 at T_C for $x = 0.125$, 0.25, and 0.375, respectively. These n values are consistent with the n values obtained from Fig. 11(a) and also from eqn (26) as tabulated in Table 2. Above T_C, the n values are found to be the increasing trend but do not cross the critical value of 2 for $x = 0.125$, 0.250, and 0.375. The minimum n values at T_C and $n < 2$ above T_C confirm the second-order phase transition which is explained by Law et al.[38] For $x = 0.00$, and 0.500 as evident from Fig. 13(a and e) it is found the anomalous behavior of n-T curves shows the minimum n values at T_C which is very different compared with that of the n values described in Sec. 3.3. This behavior for $x = 0.00$, and 0.500 is non-universal class of materials showing the non-realistic MCE values. Although n-T shows anomalous behavior, however, n values less than 2 for all the temperature suggest that the samples ($x = 0.00$, and 0.500) exhibit the second-order phase transition.

4   Conclusions

The effect of Cr^{3+} substitution on the magnetic and MCE properties of various $Co_{1-x}Cr_xFe_2O_4$ prepared by the solid–state reaction technique have been evident in this report. The Arrott plot from the analysis of M–H isotherms exhibits the second-order phase transition that has been perfectly confirmed from

the critical analysis and scaling analysis of the MCE effect. The $x = 0.125$, 0.250, and 0.375 samples demonstrate high RCP values in the range of 127–145 J kg^{-1} compared to that of other ferrites. The universal curve scaling and scaling analysis of the MCE effect confirms the universal class and the MCE values for $x = 0.125$, 0.250, and 0.375 are reliable. The higher MCE values up to 145 J kg^{-1} are observed for $x = 0.375$, which might be considered as potential candidates for the cooling technology. On the other hand, the higher microwave frequency for all compositions makes them a strong candidate for high-frequency microwave applications, especially in satellite communications and biomedical applications.

Conflicts of interest

There are no conflicts to declare.

References

1 J. Massoudi, M. Smari, K. Nouri, E. Dhahri, K. Khirouni, S. Bertaina, L. Bessais and El K. Hlil, *RSC Adv.*, 2020, **10**(57), 34556–34580.

2 N. Amri, J. Massoudi, K. Nouri, M. Triki, E. Dhahri and E. L. Bessais, *RSC Adv.*, 2021, **11**(22), 13256–13268.

3 H. Q. Alijani, S. Iravani, S. Pourseyedi, M. Torkzadeh-Mahani, M. Barani and M. Khatami, *Sci. Rep.*, 2021, **11**(1), 17431.

4 N. Kouki, S. Hcini, M. Boudard, R. Aldawas and A. Dhahri, *RSC Adv.*, 2019, **9**(4), 1990–2001.

5 S. Dudziak, Z. Ryzynska, Z. Bielan, J. Ryl, T. Klimczuk and A. Zielińska-Jurek, *RSC Adv.*, 2020, **10**(32), 18784–18796.

6 A. A. Azab, A. M. Mansour and G. M. Turky, *Sci. Rep.*, 2020, **10**(1), 4955.

7 J. Saini, M. Sharma and B. K. Kuanr, *Nanoscale Adv.*, 2021, **3**, 6074–6087.

8 A. Spivakov, C. Lin, E. Lin, Y. Chen and Y. Tseng, *Nanoscale Res. Lett.*, 2021, **16**, 162.

9 S. G. Greculeasa, P. Palade, G. Schinteie, A. Leca, F. Dumitrache, I. Lungu, G. Prodan, A. Kuncser and V. Kuncser, *Sci. Rep.*, 2020, **10**, 17174.

10 R. Ramzan, M. Tariq, M. N. Ashiq, H. Albalawi, I. Ahmad, M. H. Alhossainy, S. R. Ejaz, R. Y. Khosa, H. M. T. Farid,

H. M. Khan, T. I. Al-Muhimeedh and A. A. AlObaid, *J. Mater. Res. Technol.*, 2021, **12**, 1104–1112.

11 S. K. Gore, S. S. Jadhav, V. V. Jadhav, S. M. Patange, M. Naushad, R. S. Mane and K. H. Kim, *Sci. Rep.*, 2017, **7**, 2524.

12 S. Jauhar, J. Kaur, A. Goyal and S. Singhal, *RSC Adv.*, 2016, **6**(100), 97694–97719.

13 S. Y. Srinivasan, K. M. Paknikar, D. Bodas and V. Gajbhiye, *Nanomedicine*, 2018, **13**(10), 1221–1238.

14 S. R. Mokhosi, W. Mdlalose, A. Nhlapo and M. Singh, *Pharmaceutics*, 2022, **14**, 937.

15 D. Karthickraja, S. Karthi, G. A. Kumar, D. K. Sardar, G. C. Dannangoda, K. S. Martirosyan and E. K. Girija, *New J. Chem.*, 2019, **43**, 13584–13593.

16 C. Vázquez-Vázquez, M. Lovelle, C. Mateo, M. A. López-Quintela, M. C. Buján-Núñez, D. Serantes, D. Baldomir and J. Rivas, *Phys. Status Solidi*, 2008, **205**(6), 1358–1362.

17 E. V. Gopalan, I. A. Al-Omari, D. S. Kumar, Y. Yoshida, P. A. Joy and M. R. Anantharaman, *Appl. Phys. A*, 2010, **99**(2), 497–503.

18 A. Hai, B. Alqassem, G. Bharath, K. Rambabu, I. Othman, M. A. Haija and F. Banat, *Electrochim. Acta*, 2020, 137083.

19 S. Rehman, M. A. Ansari, M. A. Alzohairy, M. N. Alomary, B. R. Jermy, R. Shahzad, N. Tashkandi and Z. H. Alsalem, *Biomed. App.*, 2019, **7**(10), 714.

20 S. Xavier, S. Thankachan, B. P. Jacob and E. M. Mohammed, *J. Nanotechnol.*, 2013, **2013**, 1–7.

21 Y. Slimani, M. A. Almessiere, S. Guner, B. Aktas, S. E. Shirsath, M. V. Silibin, A. V. Trukhanov and A. Baykal, *ACS Omega*, 2022, **7**, 6292–6301.

22 D. Thomas, I. G. Deac, C. Oana, E. A. Levei, L. Diamandescu and G. Borodi, *J. Alloys Compd.*, 2019, **792**, 432–443.

23 M. A. Almessiere, Y. Slimani, H. Güngüneş, S. Ali, A. Manikandan, I. Ercan, A. Baykal and A. V. Trukhanov, *Nanomater.*, 2019, **9**(6), 820.

24 G. A. Lone and M. Ikram, *J. Alloys Compd.*, 2022, **908**, 164589.

25 M. A. Islam, A. K. M. Akther Hossain, M. Z. Ahsan, M. A. A. Bally, M. Samir Ullah, S. M. Hoque and F. A. Khan, *RSC Adv.*, 2022, **12**, 8502–8519.

26 B. Branka, J. Vukoman, M. Dušan, J. Zvonko, M. Darko, J. Nataša and M. Marinović-Cincović, *J. Nanomater.*, 2013, **2013**, 1–9.

27 R. B. Kamble, V. Varade, K. P. Ramesh and V. Prasad, *AIP Adv.*, 2015, **5**(1), 017119.

28 M. A. Abdullah Dar, J. Shah, W. A. Siddiqui and R. K. Kotnala, *Appl. Nanosci.*, 2014, **4**(6), 675–682.

29 E. Oumezzine, S. Hcini, M. Baazaoui, E. K. Hlil and M. Oumezzine, *Powder Technol.*, 2015, **278**, 189–195.

30 S. Hcini, N. Kouki, R. Aldawas, M. Boudard, A. Dhahri and M. L. Bouazizi, *J. Supercond. Novel Magn.*, 2018, **32**, 1085–1094.

31 N. Fortas, A. Belkahla, S. Ouyahia, J. Dhahri, E. K. Hlil and K. Taibi, *Solid State Sci.*, 2020, **101**, 106137.

32 S. Hcini, A. Dhahri, S. Zemni and M. L. Bouazizi, *J. Mater. Sci.: Mater. Electron.*, 2019, **30**, 6127–6138.

33 A. M. Tishin and Y. I. Spichkin, *The magnetocaloric effect and its applications*, IOP Publishing, ISBN, 0750309229, 2003.

34 V. Singh, P. Bag, R. Rawat and R. Nath, *Sci. Rep.*, 2020, **10**(1), 6981.

35 A. Boutahar, R. Moubah, E. K. Hlil, H. Lassri and E. Lorenzo, *Sci. Rep.*, 2017, **7**(1), 13904.

36 A. Arrott, *Phys. Rev.*, 1957, **108**(6), 1394–1396.

37 A. Arrott and A. J. E. Noakes, *Phys. Rev. Lett.*, 1967, **19**, 786.

38 J. Y. Law, V. Franco, L. M. Moreno-Ramírez, A. Conde, D. Y. Karpenkov, I. Radulov, K. P. Skokov and O. Gutfleisch, *Nat. Commun.*, 2018, **9**(1), 2680.

39 V. Franco, J. S. Blazquez and A. Conde, *Appl. Phys. Lett.*, 2006, **89**(22), 222512.

40 S. Chakrabarty, A. Dutta and M. Pal, *J. Magn. Magn. Mater.*, 2018, **461**, 69–75.

41 S. E. Shirsath, S. S. Jadhav, B. G. Toksha, S. M. Patange and K. M. Jadhav, *J. Appl. Phys.*, 2011, **110**(1), 013914.

42 M. Zhang, Z. Zi, Q. Liu, P. Zhang, X. Tang, J. Yang, X. Zhu, Y. Sun and J. Dai, *Adv. Mater. Sci. Eng.*, 2013, **2013**, 1–10.

43 C. Caizer, *Mater. Sci. Eng., B*, 2003, **100**(1), 63–68.

44 P. Mehrotra, B. Chatterjee and S. Sen, *Sens*, 2019, **19**(5), 1013.

45 L. D. Landau and E. M. Lifshitz, *Statistical Physics, "Theoretical Physics"*, Pergamon, Oxford, 1996, vol. 5.

46 B. Widom, *J. Chem. Phys.*, 1964, **41**(6), 1633.

47 J. S. Kouvel and M. E. Fisher, *Phys. Rev.*, 1964, **136**(6), A1626–A1632.